Journal of Textiles and Polymers

Vol. 13, No. 1, 3-20, Jan 2025
https://www.itast.ir
DOI: https://doi.org/10.48302/jtp.2026.573782.1346

Experimental and Numerical Investigation of Two-Way Reinforced Concrete Slabs Retrofitted with Braided Glass/Epoxy Composite Grids

Ali Shakersoureh[1], Majid Safarjohari[1*], Hadi Dabiryan[1], Farzad Hatami[2]

[1] Department of Textile Engineering, Amirkabir University of Technology, Tehran, Iran.

[2] Structural and Earthquake Research Institute, Amirkabir University of Technology, Tehran, Iran.

Article Information

Article history:

Received: 2026-02-03

Accepted: 2026-07-20

***Keywords*:**

Concrete slab, Braided composite grid, Numerical analysis, 2D braid.

Abstract

The structural integrity of concrete slabs is a vital concern in civil engineering, necessitating innovative reinforcement and retrofitting techniques to ensure their long-term performance and resilience. This study explores the use of a novel two-dimensional braided glass/epoxy composite grid for retrofitting two-way reinforced-concrete slabs. Through comprehensive numerical analysis and experimental validation, the research aims to assess the effectiveness of this advanced reinforcement technique in enhancing the mechanical properties and stress distribution of retrofitted slabs. The finite-element modeling procedure was validated experimentally using an unretrofitted control slab and a slab retrofitted with a 50×50 mm braided composite grid. A Representative Volume Element (RVE) model is employed to simulate the braided composite grid, providing insights into its advantages and potential challenges. The findings demonstrate significant improvements in load-bearing capacity, energy absorption, and overall durability, offering a promising solution for the rehabilitation of aging infrastructure. Within the investigated configurations, braided-grid retrofitting increased the ultimate load by up to 53.62%, with the maximum improvement obtained for the 105 mm-thick C35 slab strengthened using the 100×100 mm grid. This study contributes to the existing body of knowledge by highlighting the practical applications and benefits of incorporating braided composite grid in the retrofitting of concrete slabs.

1 INTRODUCTION

Concrete slabs are crucial components in modern construction, valued for their durability, versatility, and structural integrity. These flat, horizontal surfaces made of concrete are used for floors, roofs, ceilings, and pavements, known for their ability to evenly distribute loads and withstand significant pressures[1]. Various types, such as suspended slabs, ground-bearing slabs, and precast slabs, cater to different construction needs[2, 3]. The design process involves careful consideration of load-bearing capacity, thickness, reinforcement, and curing processes, with steel bars or mesh often used to enhance strength[1]. Concrete slabs can be reinforced with various materials to enhance their strength and durability. Common types of reinforcements include steel reinforcing bars (rebar), which provide significant tensile strength and improve adhesion with concrete[1]. Welded wire fabric (WWF) offers uniform tensile strength across the slab's surface. Fiber-reinforced polymers (FRP) and carbon fiber reinforcing grids are lightweight, corrosion-resistant, and provide excellent tensile strength [2, 4-6]. Glass fiber reinforced concrete (GFRC) incorporates glass fibers, offering high tensile strength and durability. Textile-based reinforcements, such as FRP and carbon fiber grids, are categorized together for their use of high-strength fibers embedded in a polymer matrix. Post-tensioned cables are used to provide additional compressive strength and control cracking in concrete slabs. These reinforcements ensure that concrete slabs can withstand tensile forces and maintain structural integrity, making them indispensable in civil engineering[7, 8]. The application of FRP in concrete slabs involves the use of fiber sheets, strips, or bars, which are bonded to the surface or embedded within the concrete. This reinforcement method helps to improve the slab's tensile strength, crack resistance, and overall durability, providing a viable alternative to traditional steel reinforcements[9]. The use of FRP in concrete slab reinforcement has gained significant attention in recent years, offering innovative solutions for both new constructions and the repair and retrofitting of existing structures[10].

Recent studies on concrete slabs have shed light on several key aspects. One study focuses on the sustainability of column-supported slabs, offering a multi-criteria assessment that includes environmental, economic, and social impacts[11]. Another research study investigates the

* Corresponding Author: Mjohari@aut.ac.ir

structural behavior of hybrid concrete slabs reinforced with carbon-fiber-reinforced polymer and steel grids, finding them to be highly effective in resisting impact loads[12]. Additionally, there's an exploration into the relationship between structural design parameters and environmental sustainability in slab construction, aiming to optimize both structural efficiency and environmental impact[13]. Comparative studies on embodied carbon in different slab designs provide insights for making environmentally conscious decisions in construction[14].

Several studies have explored various aspects of concrete slab reinforcement and retrofitting. For instance, a study on a 40-year-old viaduct with severe environmental damage assessed retrofitting techniques by replacing deteriorated concrete and reinforcing slabs in flexure, using experimental and non-destructive tests to evaluate material properties and bonding efficiency, which contributed to guidelines for FRP-retrofitted bridge deck repairs [15]. Additionally, braided composites, created using two- or three-dimensional braiding techniques with fibers such as glass, carbon, or aramid, enhance tensile strength, flexibility, and corrosion resistance, and can be designed for structural health monitoring, promoting sustainable construction practices [16]. Research also demonstrates that the arrangement of fibers significantly impacts the tensile properties of hybrid braided composite rods, highlighting the importance of strategic configurations [17]. Furthermore, Ayranci et al. [18] utilized Finite Element Method simulations and a Geometrical Mapping Approach to model the complex structure of braided composites, improving predictions of mechanical behavior and optimizing design.

Raoof et al. [19] examine the bond performance between TRM and concrete substrates. The findings suggest that the bond strength is influenced by factors such as the type of mortar, the surface preparation of the concrete, and the type of textile used. Proper surface preparation is essential for achieving a strong bond. Castillo et al.[20] present an innovative design approach for enhancing shear strength using Fiber-Reinforced Polymer (FRP) sheets and anchors. This methodology builds on established design guidelines and prior research. A significant aspect of the study is the incorporation of realistic experimental setups, which include crucial structural components such as diaphragm slabs and transverse beams. This comprehensive approach aims to provide practical insights for the seismic retrofitting of concrete structures.

The complexity of analyzing textile composites presents significant challenges. Representative Volume Element (RVE) models reduce intricate material microstructures into manageable, computationally efficient units that accurately predict bulk behavior [21, 22]. Embedding RVEs within multi-scale simulation frameworks further links microstructural details to macroscopic responses while minimizing calibration efforts [23]. Previous modeling methods for tubular braided composites have encountered significant challenges, such as accurately capturing the complex and anisotropic microstructure, high computational costs, and difficulties in applying precise boundary conditions, leading to limitations in predictive capabilities [18, 24-26]. So calculating the elastic modulus of a cylindrical fiber composite, especially with a complex braided geometry, can indeed be challenging. Using the Representative Volume Element (RVE) model is a great approach for capturing the composite's microstructural behavior. Shakersoureh et al. [27] have developed a finite-element–based mesoscale RVE model to predict the effective elastic constants of 2D biaxial and triaxial braided composites. In this framework, each braid strand is discretized into nine threads, and cyclic symmetry alongside periodic boundary conditions allows full extraction of elastic constants. Numerical methods, such as finite element analysis (FEA), are widely used to study the behavior of reinforced concrete structures. These methods enable the detailed examination of stress and strain distribution, crack propagation, and overall structural performance under various loading conditions. The use of advanced software, such as ABAQUS, allows for the implementation of complex material models and the validation of numerical results against experimental data[9].

Textile-based cementitious strengthening systems, commonly referred to as textile-reinforced concrete (TRC), textile-reinforced mortar (TRM), or fabric-reinforced cementitious matrix composites, have also been investigated for strengthening reinforced-concrete slabs. Previous studies have shown that these systems can enhance cracking resistance, post-cracking stiffness, flexural capacity, deformation capacity, and energy absorption in both one-way and two-way slabs [28-30]. The effectiveness of textile strengthening is influenced by the textile material, number of layers, grid configuration, surface treatment, and bond with the substrate [31]. Unlike conventional TRC or TRM systems, in which the textile is embedded within a cementitious matrix, the system investigated in the present study consists of hollow braided composite members arranged as a grid and bonded directly to the slab soffit using epoxy resin.

This study contributes to the existing body of knowledge by providing a comprehensive numerical analysis of concrete slabs retrofitted with a newly developed 2D braided composite grid, highlighting the advantages and potential challenges associated with this reinforcement technique. The structural performance of concrete slabs is a critical aspect of civil engineering, particularly when considering innovative reinforcement techniques. The use of a two-dimensional braided composite grid as a retrofitting material has gained attention due to its enhanced mechanical properties and improved stress distribution capabilities. In the present work, the finite element model developed previously [27] was employed to numerically evaluate how retrofitting reinforced concrete slabs with a two-dimensional braided composite grid influences their damage progression, ultimate load-bearing capacity, and absorbed energy under concentric loading.

Although braided composite grids offer a promising solution for retrofitting concrete structures such as slabs, limited research has been conducted on this topic, and their performance remains uncertain. These composites have the potential to enhance mechanical properties, such as tensile strength and flexibility, and exhibit high corrosion resistance, thereby extending the lifespan of retrofitted structures. Their lightweight nature facilitates easier handling and installation, while the robust bond between the composites and concrete ensures structural integrity. Customizable design options enable tailored solutions to optimize performance. Furthermore, their self-sensing capabilities allow for realtime structural health monitoring, contributing to improved safety and durability. Overall, these characteristics highlight the significant potential of braided composite grids in advancing sustainable and effective retrofitting practices.

2 Finite element modeling

2-1 Braided composite grid

This study introduces a novel braided grid designed as a retrofitting element for concrete structures. The inherent flexibility of the braiding process enables the production of both biaxial and triaxial architectures and also allows yarns or fibers to be introduced in the axial direction, where they can function as an internal mandrel or core during braiding. This method enables the incorporation of unidirectional fibers, embedded sensors, and other functional materials with complex geometries. In this study, two sets of braided members were arranged in mutually perpendicular horizontal and vertical directions to form a grid, as seen in Figure 1, and the resulting assembly was bonded to the bottom surface of the concrete slab using epoxy resin. This structure has significant potential for enhanced energy absorption, increased resistance to deformation, and effective crack-arresting capabilities due to the intrinsic properties of the braided composite [17, 32-35].

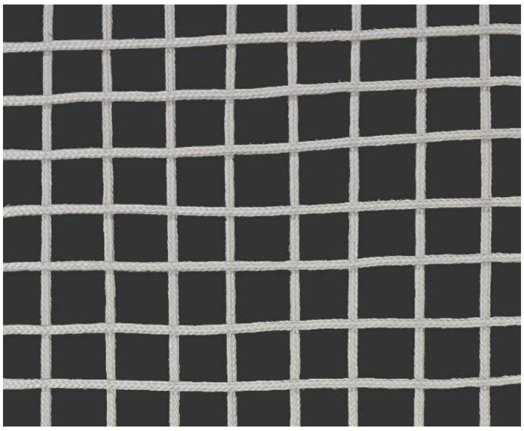

Figure 1 A view of a braided grid

In this study, two different grid densities were selected. The 50×50 mm opening was selected as a relatively dense grid configuration and was used in the experimental retrofitted specimen. The 100×100 mm opening, having twice the member spacing, was selected as a lower-density configuration to investigate the influence of grid density while maintaining the same braid geometry, material properties, and bonding condition. These openings were not selected to represent a universal concrete crack spacing, since crack spacing depends on the reinforcement, bond, material properties, and loading conditions. The braided composite grid was modeled using three-dimensional two-node linear B31 beam elements. Unlike truss elements, B31 beam elements are capable of representing axial deformation, bending, torsion, and transverse shear deformation. A hollow circular section with an outer diameter of 8.2 mm and an inner diameter of 5.8 mm was assigned to the braided members. The grid was attached to the bottom surface of the concrete slab using a tie constraint, thereby assuming perfect bond and preventing relative displacement between the composite grid and concrete. Consequently, normal and tangential actions, including interfacial shear, were transferred through the tied interface. Debonding, pull-out, and interfacial slip were not included in the present model. The intersections between the horizontal and vertical braided members were also tied together to represent the fixed connection produced by the epoxy matrix.

The braided composites were 8.20 mm in diameter. Figure 2 gives a picture of the assembly of the braided composite grid. In the structural-scale model, material direction 3 was aligned with the longitudinal axis of each B31 braided member; therefore, the experimentally validated modulus E_3 governed its primary axial response.

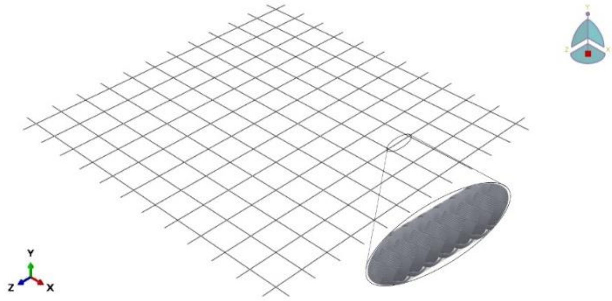

Figure 2 100×100 grid configuration

2-2 Concrete slab model

To evaluate the efficacy of braided composite grid as a retrofitting solution for the failure of reinforced concrete (RC) slabs, a finite element analysis (FEA) is conducted using ABAQUS software on a set of twelve modeled slabs. The specimens are divided into two groups according to their concrete properties. The first group consists of slabs made with C45 concrete, while the second group is composed of slabs using C35 concrete. Each specimen features a square slab with dimensions of 1200 × 1200 mm and thicknesses of either 105 mm or 65 mm. The displacement is applied using a rigid steel plate measuring 150 × 150 × 30 mm. The C35S1 slab was cast and experimentally tested in the present study as the unretrofitted control specimen. The control slab was cast using C35 concrete without any externally bonded braided composite grid. Roller supports were provided along the bottom edges of the slab to reproduce the boundary conditions of the experimental setup. As shown in Figure 3, the internal steel reinforcement was arranged as orthogonal grids in two layers. The bottom layer consisted of eleven 16 mm-diameter bars in each of the two perpendicular directions ($11\varphi16$), while the top layer consisted of eleven 6 mm-diameter bars in each direction ($11\varphi6$). A concrete cover of 15 mm was provided between each reinforcement layer and the corresponding top or bottom surface of the slab.

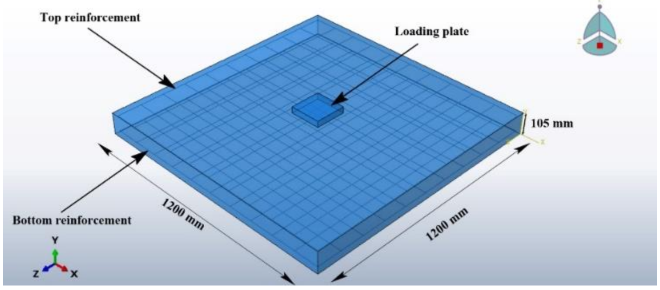

Figure 3 Concrete slab layout and reinforcement arrangements

In the numerical modeling, the selection of appropriate finite element types is essential for accurately capturing structural behavior. In this study, steel reinforcement rods were defined as truss elements, as they primarily resist axial forces (tension and compression) without contributing to significant bending behavior. Truss elements ensure computational efficiency while effectively representing the tensile role of reinforcement within the concrete matrix. Unlike steel rods, the composite grid interacts with the slab by contributing to bending, shear, and localized deflections, necessitating the use of beam elements for its numerical representation. Beam elements provide a more detailed response to flexural behavior and shear effects, making them a suitable choice for modeling the mechanical interaction between the composite reinforcement and the existing slab. This methodological approach ensures a realistic simulation of the structural performance improvements achieved through the application of the retrofitting grid.

Twelve slab specimens were modeled numerically in ABAQUS, including four control slabs and eight retrofitted slabs. The specimens incorporated two slab thicknesses, two concrete strength classes, and two FRP composite grid densities. In addition, the C35S1 control slab and the C35S1-50 retrofitted slab were fabricated and tested experimentally to validate the corresponding numerical models. Detailed specimen specifications are provided in Table 1.

2-3 Material properties

2-3-1 Concrete property

In this study, the steel reinforcing bars used consisted of ø6 and ø16 with yield strength of 420 MPa. Numerical modeling of reinforced concrete (RC) structures presents several challenges, including element representation, the implementation of appropriate constitutive models, and achieving reliable predictive accuracy. Consequently, the concrete was modeled using the Concrete Damaged Plasticity model implemented in ABAQUS, while the material-specific compressive, tensile, and damage relationships were generated using the Simplified Concrete Damage Plasticity formulation proposed by Hafezolghorani et al. [36] to simulate concrete behavior. The CDP model is extensively utilized for analyzing complex structural concrete elements reinforced or strengthened with fiber-reinforced polymer (FRP) materials, encompassing beams [37-39], columns [40, 41], and slabs [42, 43]. The concrete properties incorporated in this study had compressive strengths of 35 MPa and 45 MPa. To comprehensively define the concrete damaged-plasticity (CDP) model, five key parameters must be specified. The values assigned to these parameters are presented in Table 2.

The concrete behavior was simulated using the Concrete Damaged Plasticity (CDP) model available in ABAQUS. The CDP parameters presented in Table 2 and the material-specific compression, tension, and damage relationships were adopted or generated following the Simplified Concrete Damage Plasticity (SCDP) formulation proposed by Hafezolghorani et al.[36]. This formulation provides a simplified procedure for generating the material input data required by the ABAQUS CDP model for different concrete compressive strengths.

The dilation angle, flow-potential eccentricity, ratio of biaxial to uniaxial compressive yield stress, and yield-surface parameter were adopted from Hafezolghorani et al. [36]. The general uniaxial damaged-plasticity relationships in compression and tension are expressed as:

$$\sigma_c = (1 - d_c)E_0\left(\varepsilon_c - \varepsilon_c^{pl}\right) \quad (1)$$

$$\sigma_t = (1 - d_t)E_0\left(\varepsilon_t - \varepsilon_t^{pl}\right) \quad (2)$$

where E_0 is the initial elastic modulus, σ_c and σ_t are the uniaxial compressive and tensile stresses, ε_c and ε_t are the corresponding total strains, ε_c^{pl} and ε_t^{pl} are the equivalent plastic strains, and d_c and d_t are the compressive and tensile damage variables, respectively. The damage variables vary between zero for undamaged concrete and unity for complete stiffness degradation.

The uniaxial compressive stress-strain response was generated using the Kent-Park parabolic relationship adopted in the SCDP formulation:

Table 1 Details of test specimens

Specimen code	type	Slab thickness	Concrete type	Retrofitting grid opening
C35S1	control	105	C35	-
C45S1	control	105	C45	-
C35S1-100	Retrofitted slab	105	C35	100×100
C35S1-50	Retrofitted slab	105	C35	50×50
C45S1-100	Retrofitted slab	105	C45	100×100
C45S1-50	Retrofitted slab	105	C45	50×50
C35S2	control	65	C35	-
C45S2	control	65	C45	-
C35S2-100	Retrofitted slab	65	C35	100×100
C35S2-50	Retrofitted slab	65	C35	50×50
C45S2-100	Retrofitted slab	65	C45	100×100
C45S2-50	Retrofitted slab	65	C45	50×50

Table 2 Concrete damaged plasticity parameters adopted from Hafezolghorani et al.[36], with a modified viscosity coefficient

Dilation angle	Eccentricity	f_{bo}/f_{co}	K	Viscosity parameter
31	0.1	1.16	0.667	0.001

$$\sigma_c = f_c\left[2\left(\frac{\varepsilon_0}{\varepsilon_{c0}}\right)-\left(\frac{\varepsilon_0}{\varepsilon_{c0}}\right)^2\right] \quad (3)$$

where fc is the uniaxial compressive strength, and the strain corresponding to the peak compressive stress was taken as:

$$\varepsilon_{c0} = 0.002 \quad (4)$$

The compressive inelastic strain required as input in ABAQUS was determined as:

$$\varepsilon_c^{in} = \varepsilon_c - \frac{\sigma_c}{E_0} \quad (5)$$

In compression, the damage parameter remained zero throughout the ascending branch up to the peak compressive strength:

$$d_c = 0\,, \qquad \sigma_c \le f_c$$

Compression damage was initiated during the post-peak softening response after the concrete reached its peak compressive stress. The evolution of compression damage was defined as:

$$d_c = 1 - \frac{\sigma_c}{f_c} \quad (6)$$

In the adopted Concrete Damaged Plasticity formulation, tensile and compressive damage initiation and evolution were defined through the material-specific constitutive and damage relationships rather than through a separate independent damage-initiation criterion. Tensile inelasticity was initiated when the tensile stress reached the concrete tensile strength ft, which was defined using the simplified relationship proposed by Hafezolghorani et al. [36]:

$$f_t = 0.1\, f_c \quad (7)$$

Accordingly, the tensile strengths of C35 and C45 concrete were taken as 3.5 MPa and 4.5 MPa, respectively. At this point, the tensile damage parameter was dt=0. Following tensile cracking, the tensile stress decreased according to the specified tension-softening relationship, while the tensile damage variable evolved according to:

$$d_t = 1 - \frac{\sigma_t}{f_t} \quad (8)$$

The tensile cracking strain was calculated as:

$$\varepsilon_t^{ck} = \varepsilon_t - \frac{\sigma_t}{E_c} \quad (9)$$

The numerical tensile failure condition was taken as dt=0.99, corresponding to a residual tensile stress equal to approximately 1% of the initial tensile strength. Numerical failure was therefore identified when dt=0.99 was reached in the critical tensile region beneath the slab.

The same general CDP plasticity parameters were used for C35 and C45 concrete because these parameters define the plastic flow potential and the general shape of the yield surface. However, the two concrete grades were assigned different material-specific elastic, compressive, tensile, and damage responses. These responses were generated separately by substituting the corresponding compressive strengths, fc=35 MPa and fc=45 MPa, into the SCDP constitutive relationships.

The resulting data were subsequently entered into ABAQUS as separate compression-hardening, compression-damage, tension-stiffening, and tension-damage tables for C35 and C45 concrete. The properties were calculated using the equations and assumptions of the SCDP formulation and were then defined in the ABAQUS material model.

For C35 and C45 concrete, the compressive strength, elastic modulus, Poisson's ratio, and tensile strength are presented in Table 3. The tensile strengths were calculated using ft=0.1fc, while the hardening, softening, and damage relationships were generated from the SCDP constitutive equations presented above.

Table 3 Material properties of C35 and C45 concrete

Concrete	f_c (MPa)	E_c (GPa)	v	f_t (MPa)
C35	35	28	0.2	3.5
C45	45	31.8	0.2	4.5

Both tensile and compressive damage were included in the concrete material model. Nevertheless, because the braided composite grid was attached to the bottom surface of the slab, the present study primarily focused on tensile cracking and tensile stiffness degradation below the neutral axis. Accordingly, the numerical damage discussion was based mainly on the DAMAGET contours, while detailed interpretation of the DAMAGEC contours at the upper compressive face was outside the primary scope of the present work. Also, the two concrete strengths were selected to investigate the influence of substrate strength on the structural response and efficiency of braided-grid retrofitting. The selected values represent practically relevant normal-strength concretes with sufficient integrity to transfer stresses to the externally attached composite grid. Lower-strength concretes were not considered because premature substrate damage could dominate the response and obscure the mechanical contribution of the retrofitting system.

2-3-2 Braided grid property

The parameters and dimensions of the braided representative volume element (RVE) model are detailed in Tables 4 and 5, as referenced in [27]. At the microscale, each braided strand was represented by nine individual glass-fiber yarns, each having a linear density of 100 Tex, interlaced in a 16-carrier braiding machine to form a hollow braided structure with a regular braid pattern and a braid angle of 30º, as shown in Figure 4. The effective orthotropic elastic constants of the biaxial braided composite were obtained using the multiscale RVE-FEM framework developed by Shakersoureh et al. [27] as presented in Table 6. In the study, cyclic symmetry and periodic boundary conditions were applied under six independent loading modes to determine the complete effective stiffness tensor of the braided composite. It has been observed that the relative errors for the RVE model are quite small. Comparison with the experimental results reported in the study showed differences of 4.5%, 4.2%, and 5.6% for E_3, v_{23}, and G_{23}, respectively.

Table 4 Properties of materials used in RVE FEM analysis [27]

Material	Linear density (Tex)	Density (g/cm³)	Tensile strength (MPa)	Elastic modulus (MPa)	Shear modulus (MPa)	Poisson's Ratio
Glass Fiber	100	2.48	3300	69000	27000	0.2
Epoxy Resin	-	1.11	74.63	2740	2100	0.3

Table 5 Geometrical characteristics of biaxial RVE model [27]

Sample	Braid angle (°)	Inner diameter (mm)	Outer diameter (mm)	Height (mm)	Fiber volume fraction
RVE (biaxial)	30	5.80	8.20	4.75	0.40

Table 6 Predicted elastic constants of reinforced braided composite [27]

	E_1 (MPa)	E_2 (MPa)	E_3 (MPa)	ν_{12}	ν_{13}	ν_{23}	G_{12} (MPa)	G_{13} (MPa)	G_{23} (MPa)
RVE	3400	4230	12390	0.26	0.28	0.24	2070	1060	2320

Figure 4 The utilized RVE model of braided composite

3 Experimental program

3-1 Sample preparation

3-1-1 Concrete preparation

As mentioned above, two reinforced concrete slabs were fabricated and experimentally tested to validate the finite-element modeling procedure. The first specimen C35S1 was an unretrofitted control slab, while the second specimen C35S1-50 had the same dimensions, concrete properties, and internal reinforcement arrangement but was retrofitted at its bottom surface using a braided composite grid with an opening size of 50×50 mm. Both specimens had a thickness of 105 mm.

The internal steel reinforcement cages were assembled and positioned within the formwork before casting. Concrete was subsequently placed and compacted to obtain a uniform specimen, as shown in Figure 5. The slabs were then maintained under the adopted curing conditions until the completion of the 28-day preparation and curing period. The concrete used had a compressive strength of 35 MPa and a mix proportion as in Table 7.

(a)

(b)

Figure 5 a) internal steel reinforcement arrangement and b) casted concrete specimen

Table 7 Concrete mix proportion and strength

F′c (MPa)	W/C	S/S+G	d_{max} (mm)	W (kg/m3)	C (kg/m3)	S (Kg/m3)	G (Kg/m3)
35	0.6	45	20	175	292	775	962

W:Water , C:Cement , S:Sand , G: Gravel , d_{max} :Maximum gravel size in the mixture

3-1-2 Braid retrofitting system

As described previously, the braid members were manufactured continuously from glass-fiber yarns using a 16-carrier braiding machine with a braid angle of 30º. For installation of the retrofitting grid, the concrete slab was inverted to provide access to its bottom surface, and the surface was prepared. The continuous braided member was then routed across the slab soffit at 50 mm center-to-center intervals in the two orthogonal directions, forming the 50×50 mm grid configuration shown in Figure 6. The installed braid was thoroughly impregnated and bonded to the concrete surface using ML-506 epoxy resin, after which the strengthened specimen was maintained under suitable conditions for a three-day curing period before testing.

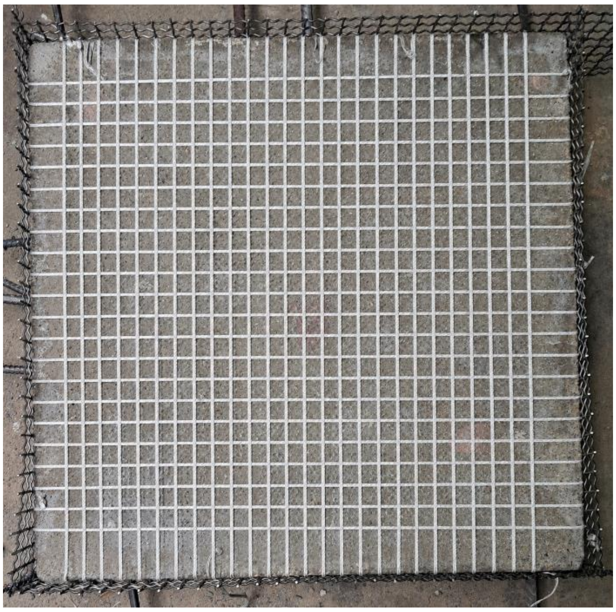

Figure 6 Prepared Concrete sample for retrofitting by braid grid

3-2 Test procedure

The slab tests were conducted with reference to ASTM E2322-22. Both slabs were subjected to monotonic concentric loading at the center of the slab under displacement control, with identical support and instrumentation conditions according to Figure 7(a). The actuator displacement was increased at a constant rate of 1 mm/min until failure, while the applied force and central slab deflection were recorded continuously. Crack initiation, crack propagation, stiffness degradation, and the final damage patterns were also documented during testing. Vertical displacement was monitored using a linear variable displacement transducer (LVDT) with a measurement range of 50 mm. The transducer was positioned at the center of the slab's soffit, directly beneath the loading point, where the maximum vertical deflection was expected to occur. Before testing, the LVDT was zeroed, and its recorded displacement was used to construct the load–displacement response of each specimen. In addition, two strain gauges were bonded to the central region of the bottom concrete surface and aligned along the two orthogonal slab directions (shown in Figure 7 (b)). These gauges were used to monitor the development of tensile strains in both principal directions and to evaluate the two-way flexural response of the slab during loading.

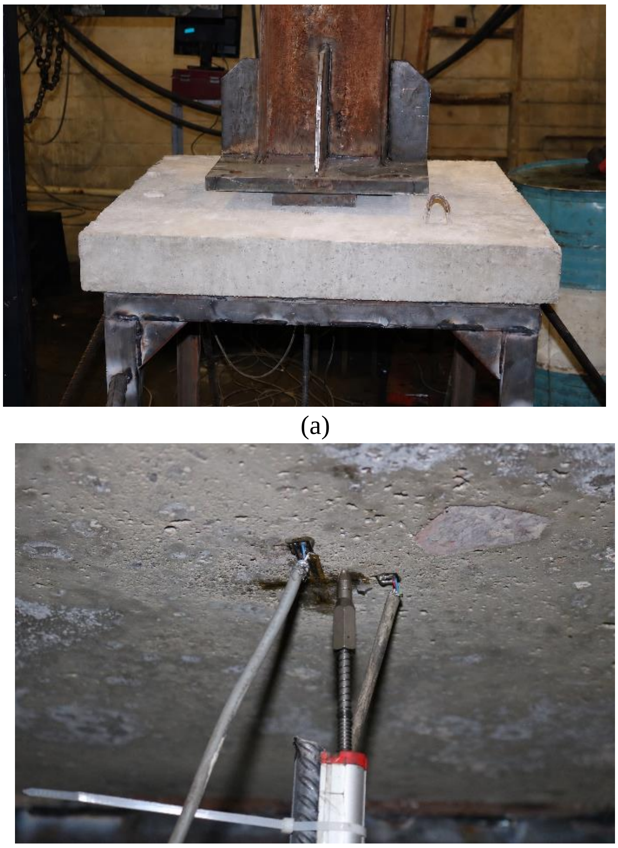

(a)

(b)

Figure 7 a)Test setup for loading of slabs and b)arrangement of the LVDT and strain gauges on the bottom surface of the concrete sample

The compressive strength of the concrete was determined using cylindrical concrete specimens tested in accordance with ASTM C39/C39M. The experimental control specimen was used to validate the numerical representation of concrete, internal steel reinforcement, support conditions, and loading arrangement. The experimental retrofitted specimen was used to validate the complete strengthened model, including the structural contribution of the braided composite grid and the assumed connection between the grid and the concrete surface. Accordingly, the finite-element model was validated using the experimental results of both specimens.

The validation was performed by comparing the numerical and experimental load–displacement responses, initial stiffnesses, ultimate loads, displacements at ultimate load, absorbed energies, and observed damage distributions.

Additionally, a mesh study was conducted to evaluate the performance of the finite element (FE) model, utilizing 8-node linear brick elements. The interface between the concrete and composite grid was modeled to simulate bonding behavior.

3-3 Mesh sensitivity study

A mesh-sensitivity study was performed using eight-node linear brick elements for the concrete slab. The maximum von Mises stress did not vary monotonically with mesh refinement. This behavior is associated with the localized nature of the reported stress and the nonlinear redistribution of stresses following concrete cracking and stiffness degradation. Refining the mesh can alter the predicted crack path and the location of the element containing the maximum stress; therefore, a pointwise stress maximum is more mesh-sensitive than a global structural quantity.

The pronounced reduction obtained for the mesh containing 106,891 nodes is interpreted as a redistribution of the localized stress field following damage initiation. With further refinement, the maximum stress approached values of 83.42 and 85.11 MPa for meshes containing 188,422 and 237,618 nodes (presented in Table 8), respectively. The difference between these two finest meshes was approximately 2.0%. Consequently, the mesh containing 188,422 nodes and 156,106 elements was selected as a suitable balance between numerical stability and computational cost.

Table 8 Results of the mesh-sensitivity study based on the maximum local von Mises stress

Number of nodes	69910	82794	106891	188422	237618
Number of elements	54280	64744	86777	156106	201467
Maximum Mises stress (MPa)	102.7	111.7	74.73	83.42	85.11

4 Results and discussion

The results are presented in two stages. First, the finite-element modeling procedure is validated against the experimentally tested unretrofitted specimen C35S1 and the retrofitted specimen C35S1-50. The experimental and numerical responses are compared in terms of load–deflection behavior, ultimate load, deflection at ultimate load, and absorbed energy. Subsequently, the validated model is used to investigate the effects of slab thickness, concrete compressive strength, and braided-grid opening size on the structural response of the slabs.

The absorbed energy (U), was calculated as the area under the load–deflection curve using the trapezoidal integration method:

$$U = \int P\, d\delta \approx \sum_{i=1}^{n-1} \frac{P_i + P_{i+1}}{2} (\delta_{i+1} - \delta_i) \qquad (10)$$

where P_i and δ_i are the measured or calculated load and deflection at each data point. For experimental–numerical comparisons, both curves were integrated over the same deflection interval to avoid errors caused by different terminal deflections.

4-1 Retrofitting Concrete Slab

Figures 8 and 9 compare the experimental load–deflection responses of the control and retrofitted slabs with the corresponding finite-element results. The control specimen C35S1 was used to assess the numerical representation of the reinforced concrete slab, including the concrete constitutive response, internal steel reinforcement, loading arrangement, and support conditions. The retrofitted specimen C35S1-50 was used to assess the complete strengthened model, including the structural contribution of the braided composite grid and the assumed grid-to-concrete connection. For specimen C35S1-50, the experimental and numerical ultimate loads were 323.67 and 341.69 kN, respectively, corresponding to a difference of 5.57%. The associated deflections at ultimate load were 4.655 and 4.593 mm, with a difference of 1.33%. These results indicate that the finite-element model reproduced the ultimate load and the associated deflection with acceptable accuracy.

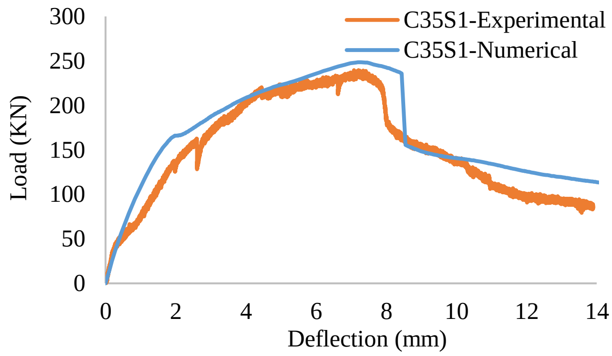

Figure 8 Comparison of the experimental and numerical load–deflection responses of the unretrofitted control slab C35S1

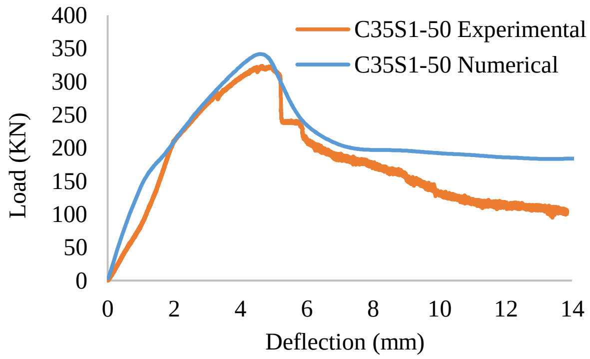

Figure 9 Comparison of the experimental and numerical load–deflection responses of the C35S1-50 slab retrofitted with a 50×50 mm braided composite grid

To quantify the difference between the complete curves, the areas under the experimental and numerical load–deflection responses were calculated using the trapezoidal rule over the common displacement interval ending at 14 mm. The resulting absorbed energies were 2764.42 J for the experimental specimen and 2926.60 J for the numerical model, corresponding to a difference of 5.87%. Therefore, the numerical model reproduced the peak load and corresponding deflection with good accuracy but overestimated the post-peak residual response and total absorbed energy. This discrepancy is attributed mainly to the assumed perfect bond between the braided grid and concrete, together with the omission of interfacial slip, local debonding, and experimental imperfections. The model is consequently considered suitable for comparative parametric analysis, while its post-peak energy predictions should be interpreted with appropriate caution since the numerical model maintained a higher residual load after the peak response than the experimental specimen. Despite this difference in the post-peak region, the model adequately reproduced the principal experimental response and was considered suitable for the comparative parametric investigation. Table 9 presents the experimental–numerical validation results in terms of ultimate load, P_u, deflection at ultimate load, δ_u, and absorbed energy evaluated over the common deflection interval, U.

This study employs a comprehensive numerical investigation using Abaqus to assess the performance of retrofitted reinforced concrete slabs. Advanced continuum damage mechanics models were implemented to capture both the cumulative damage (expressed as damageT) and the localized stiffness degradation (SDEG) resulting from crack initiation and propagation. The global structural behavior was concurrently evaluated using load–deflection diagrams and bar charts reflecting ultimate load and energy absorption. To further assess the efficacy of the various retrofitting methods, the maximum loads and absorbed energy recorded for the tested specimens were compared, as illustrated in Figures 10 and 11. The interplay between concrete strength (C35 vs. C45), slab thickness, and grid opening size proves critical in understanding and optimizing retrofitting strategies.

Table 9 Experimental–numerical validation results

Specimen	Experimental			Numerical		
	P_{ult}	δ_u	U	P_{ult} (KN)	δ_u	U
C35S1	239.23	7.21	2157.64	248.53	7.28	2380.94
C35S1-50	323.67	4.655	2764.42	341.69	4.593	2926.60

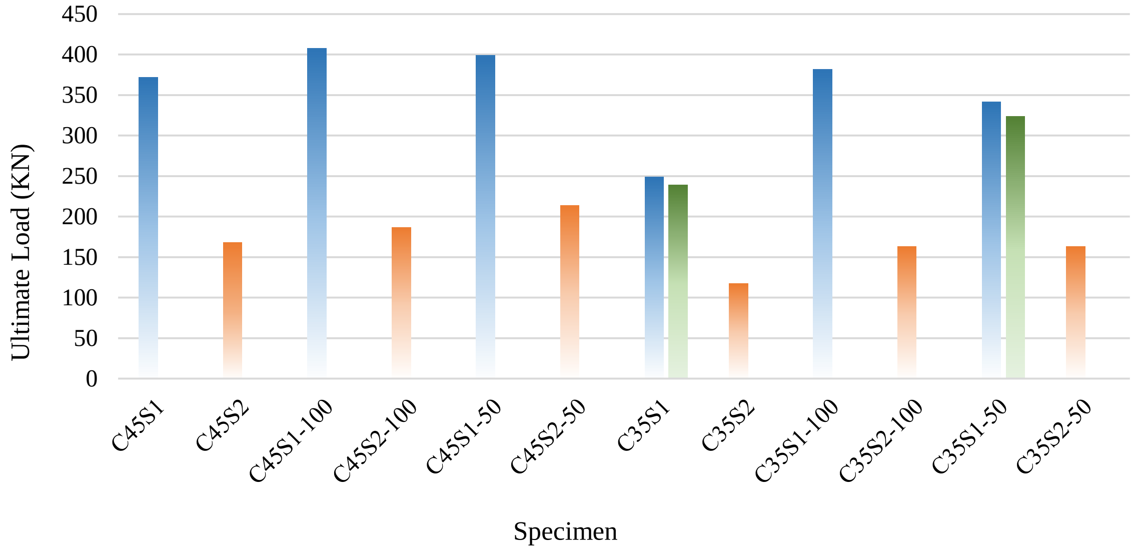

Figure 10 Maximum load carried by the concrete slab specimens

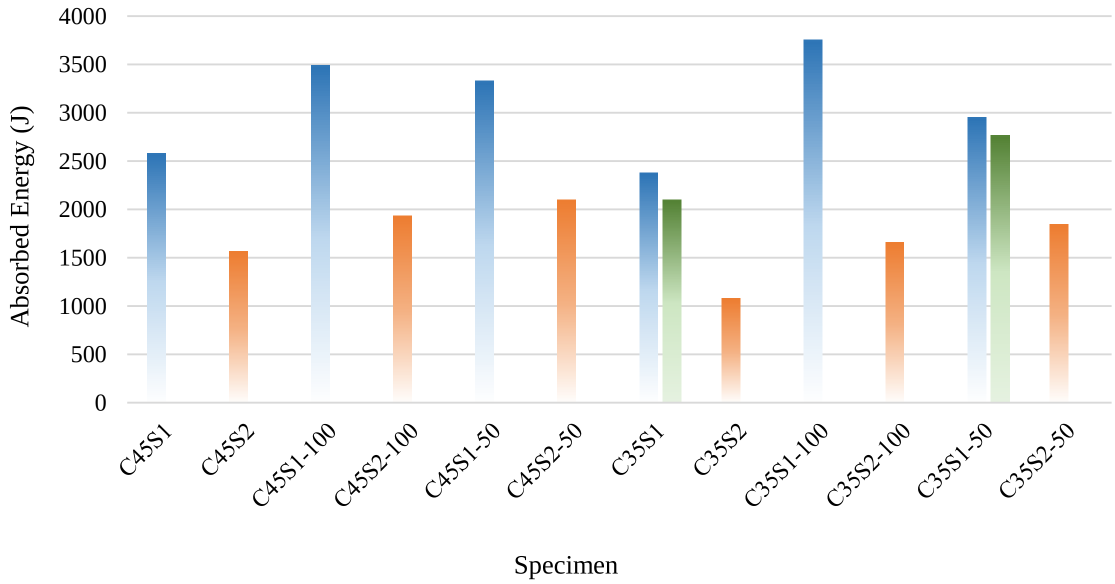

Figure 11 Absorbed energy of the concrete slab specimens

The strengthening efficiency was evaluated relative to the corresponding unretrofitted control specimen rather than only through comparison of the absolute values. The relative improvements in ultimate load and absorbed energy were calculated as:

$$\Delta P_u(\%) = \frac{P_{u,retrofitted} - P_{u,control}}{P_{u,control}} \times 100 \quad (11)$$

$$\Delta U(\%) = \frac{U_{retrofitted} - U_{control}}{U_{control}} \times 100 \quad (12)$$

These normalized measures distinguish the contribution of the braided grid from the higher baseline capacity produced by increasing the slab thickness or concrete strength. The absolute and normalized results are reported together in Table 10. For all experimental–numerical comparisons, the absorbed energy was calculated by integrating the corresponding load–deflection curves up to a common deflection limit of 14 mm, thereby ensuring that the results were evaluated under identical conditions. The results indicate an interaction between slab thickness and braided-grid opening within the investigated parameter levels. For the 105 mm-thick C35 slabs, the 100×100 mm grid produced greater improvements in both ultimate load and absorbed energy than the 50×50 mm grid. In contrast, for the 65 mm-thick C35 slabs, both grid configurations produced nearly identical increases in ultimate load, while the 50×50 mm grid provided the greater increase in absorbed energy. A similar thickness-dependent response was observed for the C45 slabs: the 100×100 mm grid was slightly more effective for the 105 mm-thick slabs, whereas the 50×50 mm grid produced greater improvements in both ultimate load and absorbed energy for the 65 mm-thick slabs. These findings show that the influence of grid opening was not constant for the two slab thicknesses and should therefore not be assessed independently of slab thickness and concrete strength.

Table 10 shows that the influence of grid opening depended on both slab thickness and concrete strength. For the 105 mm-thick C35 slabs, the 100×100 mm grid produced increases of 53.62% in ultimate load and 57.73% in absorbed energy, whereas the corresponding increases for the 50×50 mm grid were 37.48% and 24.12%, respectively. For the 65 mm-thick C35 slabs, both grid configurations produced nearly identical ultimate-load improvements; however, the 50×50 mm grid resulted in a substantially greater increase in absorbed energy, reaching 70.70%.

The relative improvements were smaller for the 105 mm-thick C45 slabs, indicating that the contribution of the braided grid decreased as the baseline concrete capacity increased. Nevertheless, for the 65 mm-thick C45 slabs, the 50×50 mm grid increased the ultimate load and absorbed energy by 27.00% and 34.06%, respectively, which were considerably greater than the improvements obtained using the 100×100 mm grid. These results confirm that the effect of grid opening cannot be evaluated independently of slab thickness and concrete strength.

Furthermore, the stress distribution within both the steel bars and the braided composite grid is depicted in Figure 12. The maximum von Mises stress recorded was 420 MPa, indicating that the steel reinforcement reached its yield stress. This observation confirms the adequacy of the reinforcement in mobilizing its full capacity under the applied loads.

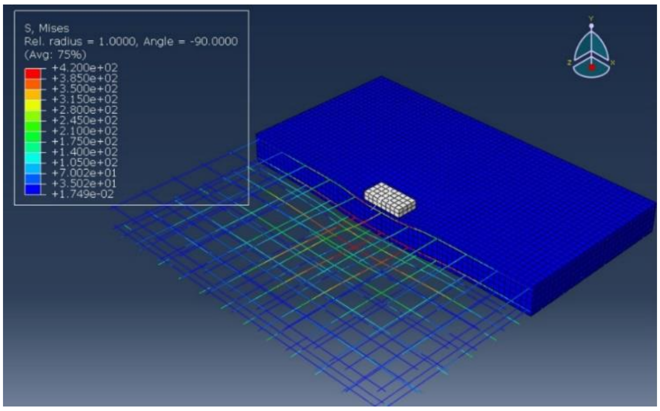

Figure 12 Stress distribution on the steel rods and braided composite grid

Table 10 Ultimate-load and absorbed-energy improvements produced by braided-grid retrofitting

Specimen	concrete	Thickness (mm)	Grid opening (mm)	Ultimate load (kN)	$\Delta P_u(\%)$	Absorbed energy (J)	$\Delta U(\%)$
C35S1	C35	105	Control	248.53	-	2380.94	-
C35S1-100	C35	105	100×100	381.80	53.62	3755.53	57.73
C35S1-50	C35	105	50×50	341.69	37.48	2955.18	24.12
C35S2	C35	65	Control	117.37	-	1080.94	-
C35S2-100	C35	65	100×100	162.93	38.82	1663.22	53.87
C35S2-50	C35	65	50×50	163.2	39.05	1845.17	70.70
C45S1	C45	105	Control	372.12	-	3296.45	-
C45S1-100	C45	105	100×100	408.02	9.65	3488.74	5.83
C45S1-50	C45	105	50×50	398.86	7.19	3332.40	1.09
C45S2	C45	65	Control	167.96	-	1567.26	-
C45S2-100	C45	65	100×100	186.47	11.02	1932.67	23.32
C45S2-50	C45	65	50×50	213.31	27.00	2101.01	34.06

4-1-1 Effect of slab thickness

The numerical analysis highlights the significant role of slab thickness in determining the load-bearing capacity and toughness of retrofitted concrete slabs. Thicker slabs inherently possess superior mechanical properties due to their increased cross-sectional depth, which facilitates more effective stress redistribution and delays the onset of localized damage. When retrofitted with a braided composite grid, thicker slabs exhibit more uniform stiffness degradation and widespread damage distribution, as seen in the SDEG and damageT contours in Table 11. The table presents the tensile-damage (DAMAGET) and stiffness-degradation contours used to evaluate the location and progression of tensile damage in the concrete slabs. Numerical failure was identified when DAMAGET reached 0.99 in the critical tensile zone beneath the slab. This behavior contrasts with thinner slabs, where stress concentrations are more pronounced, leading to localized stiffness loss and potential brittle failure if not properly retrofitted.

The findings indicate that retrofitting concrete slabs with a braided composite grid leads to a substantial increase in load-bearing capacity, with enhancements reaching up to 54%, as observed in the case of specimen C35S1-100. This remarkable improvement underscores the effectiveness of the retrofitting approach. Moreover, higher concrete compressive strength and increased slab thickness contribute to greater ultimate load capacity and absorbed energy. For the investigated 65 mm-thick slabs, reducing the grid opening from 100×100 to 50×50 mm generally increased the absorbed energy and, depending on the concrete strength, also increased the ultimate load. The results demonstrate that thicker slabs exhibit superior structural performance, with increased ultimate load capacity and energy absorption, particularly when retrofitted with composite grids featuring larger opening sizes. This enhancement is attributed to the improved stress redistribution, shear resistance, and gradual stiffness degradation, all of which contribute to a more ductile failure mechanism.

The failure mechanism of thinner slabs tends to be dominated by bending-induced flexural cracks. In contrast, thicker slabs are more susceptible to localized punching shear failure, especially when subjected to a central concentrated load. The DAMAGEDT contours of non-retrofitted thick slabs typically show a pronounced damage zone directly under the loading point, indicating a tendency toward brittle punching failure. However, retrofitting with a braided composite grid alters this behavior by redistributing stresses, reducing peak damage intensity, and delaying failure. The results demonstrate that the influence of grid opening was dependent on slab thickness. Within the investigated 105 mm-thick specimens, the 100×100 mm grid produced higher ultimate loads than the corresponding 50×50 mm configuration. In contrast, the response of the 65 mm-thick slabs showed a different sensitivity to grid opening. This behavior demonstrates an interaction between slab thickness and grid configuration; therefore, the effect of grid opening should not be interpreted independently of slab thickness.

The DAMAGET contours represent degradation of the tensile elastic stiffness and were used to identify the location and progression of tensile damage. The SDEG output represents the overall scalar stiffness-degradation state and was not interpreted as a direct crack-width measurement. To permit meaningful comparison, the contours were evaluated using the same viewing orientation, legend range, and averaging settings. Because the specimens reached different ultimate loads, a larger damaged region at the ultimate state does not necessarily indicate poorer retrofit performance; it may also reflect the greater load and energy sustained by the strengthened specimen before failure. Stresses and crack pattern propagation were observed at each loading increment up to a displacement of 14 mm. The impact of each strengthening system on the structural behavior of the tested slabs was evaluated by comparing the retrofitted specimens with the control slabs.

Figure 13 presents the final soffit conditions of the experimentally tested control and retrofitted slabs, while the corresponding numerical tensile-damage and stiffness-degradation distributions are presented in Table 11. The unretrofitted C35S1 specimen exhibited a dense network of cracks originating from the centrally loaded region and propagating radially toward the slab boundaries. Wide cracks, concrete fragmentation, and localized surface deterioration were concentrated around the central loading region. This experimental pattern agrees qualitatively with the numerical DAMAGET contour of C35S1, which predicts a highly damaged central zone together with radial bands of tensile damage extending outward. The corresponding SDEG contour similarly indicates that the greatest stiffness degradation occurred beneath and around the loading area.

(a)

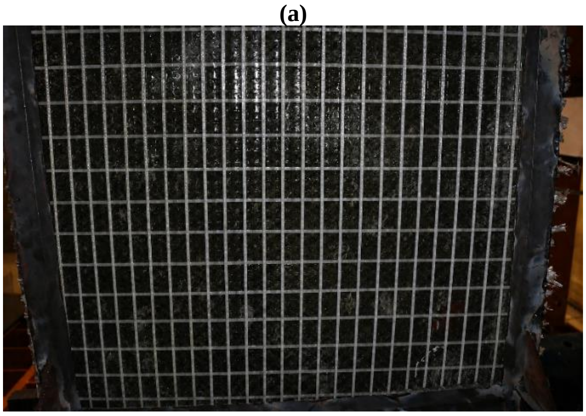

(b)

Figure 13 Final soffit damage patterns of the experimentally tested slabs: (a) unretrofitted control specimen C35S1 and (b) specimen C35S1-50 retrofitted with a 50×50 mm braided composite grid

Table 11 DamageT and SDEG contours of the specimens

specimen	damageT	SDEG
C35S1	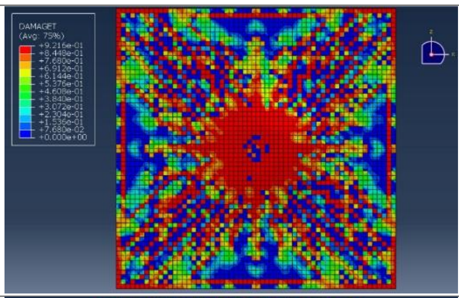	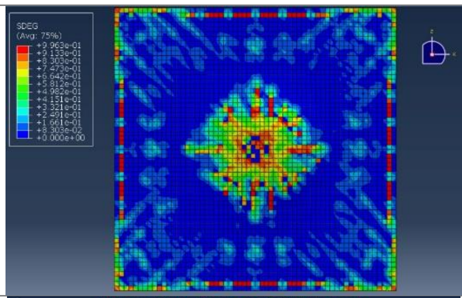
C35S1-100	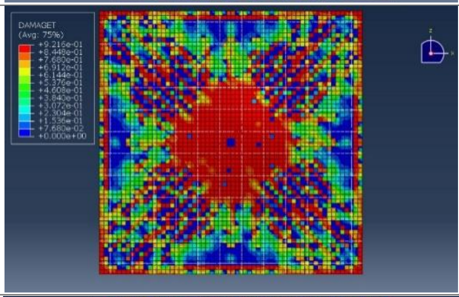	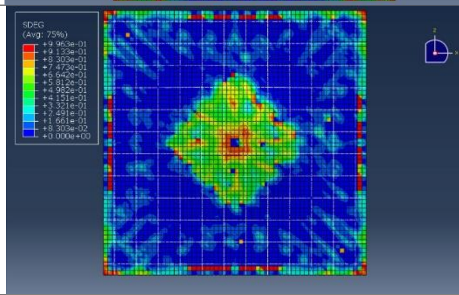
C35S1-50	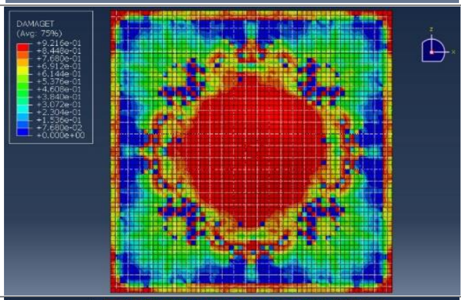	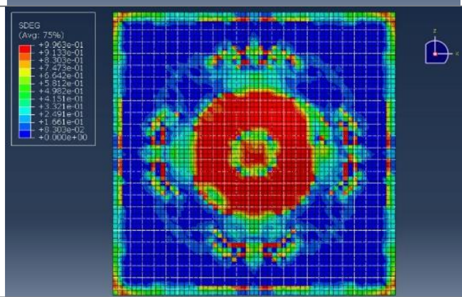
C45S1	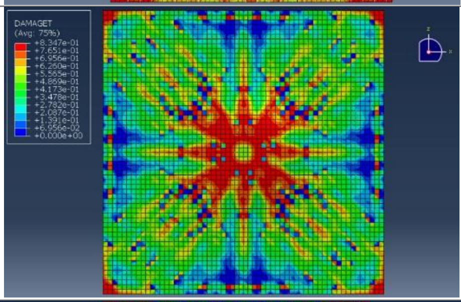	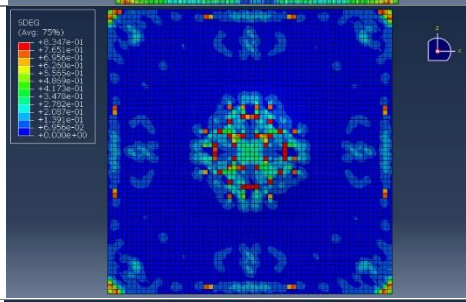
C45S1-100	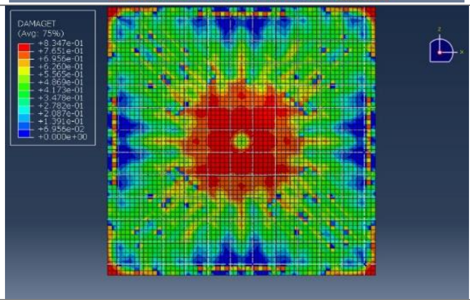	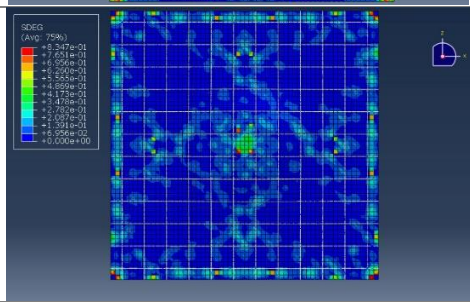
C45S1-50	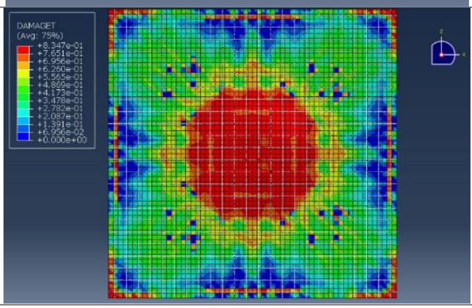	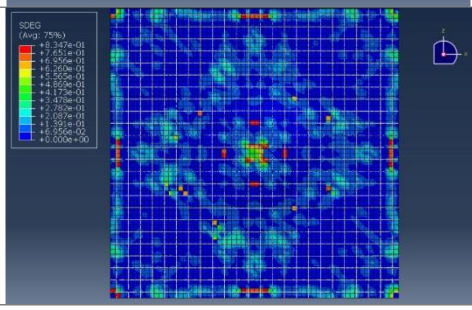

specimen	damageT	SDEG
C35S2	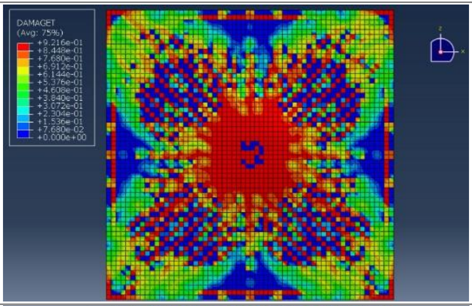	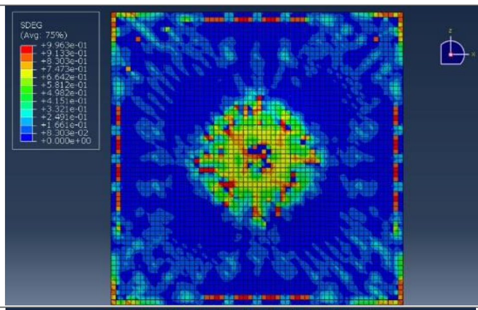
C35S2-100	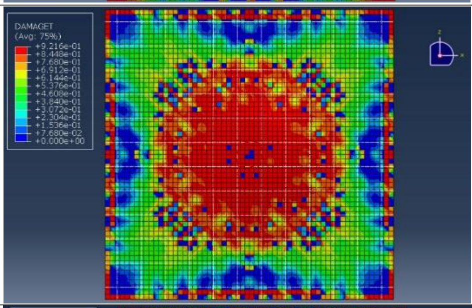	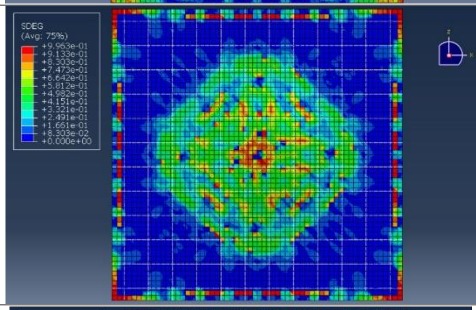
C35S2-50	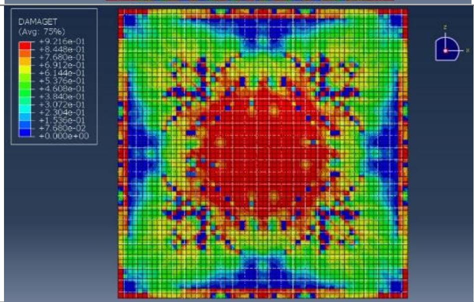	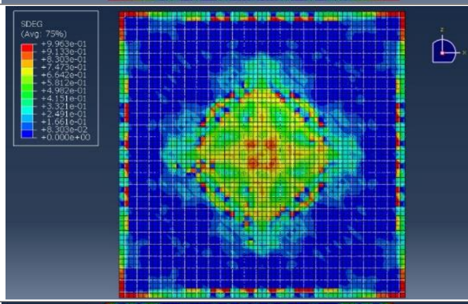
C45S2	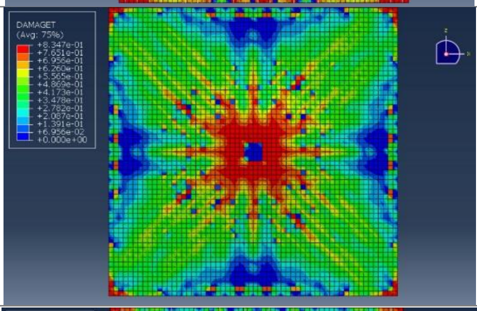	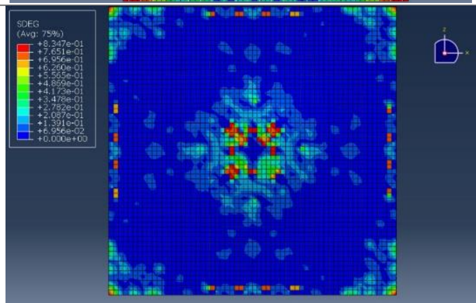
C45S2-100	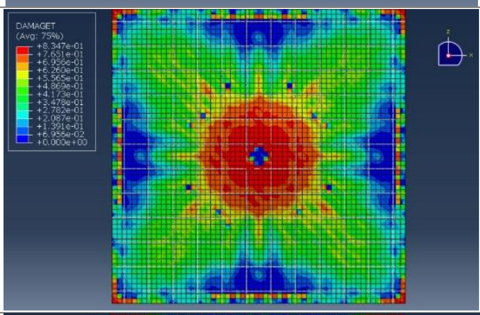	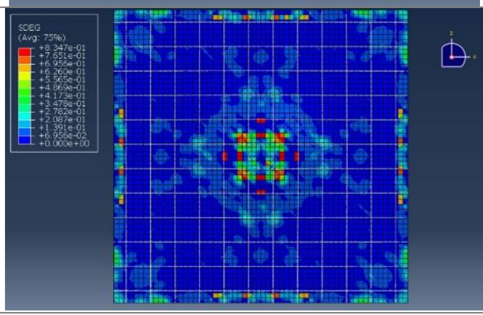
C45S2-50	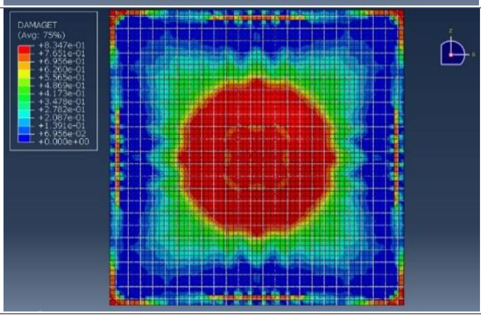	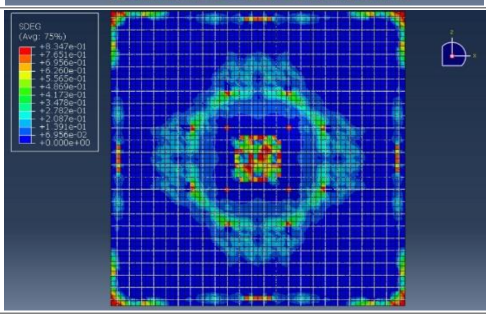

In the retrofitted C35S1-50 specimen, the braided composite grid remained distributed over the slab soffit after testing, and no comparable network of widely opened radial cracks was visible on the exposed surface. The grid and epoxy layer partially obscured direct observation of the underlying concrete cracks; nevertheless, the photograph indicates that the retrofit maintained continuity across the damaged region and prevented the development of the large, separated concrete fragments observed in the control specimen. The numerical results for C35S1-50 show a broader and approximately circular tensile-damage region around the loading area, with stiffness degradation redistributed through the surrounding grid-reinforced zone. Therefore, both the experimental and numerical observations indicate that the braided grid modified the damage pattern from concentrated radial cracking toward a more distributed central damage mechanism. This comparison is qualitative because the epoxy-impregnated grid concealed part of the concrete surface and the numerical model assumed a perfect grid-to-concrete bond.

Comparison of the control and retrofitted specimens indicates that the braided grid delayed the concentration of critical tensile damage beneath the loading region and promoted a more distributed degradation pattern. However, the contour results should be interpreted together with the global load–deflection response. Numerical failure was defined by the attainment of dt=0.99 within the critical tensile region together with the peak and subsequent degradation of the global load-carrying response, rather than by the occurrence of dt=0.99 at a single isolated integration point. The load–displacement diagrams (Figure 14) reinforce these observations, showing that retrofitted thicker slabs sustain higher ultimate loads and absorb greater energy before failure, resulting in a more ductile failure progression. In configurations such as C35S1-100, the gradual stiffness degradation observed in SDEG contours and extended post-peak behavior in load–displacement response confirm that thicker slabs not only achieve superior performance but also benefit more from larger grid opening sizes, which enhance load redistribution. However, for thinner slabs, retrofitting is more critical, as it prevents early crack propagation and helps mitigate stress concentration effects, particularly when smaller grid openings are used to improve localized stiffness retention. These findings underscore that slab thickness is a fundamental factor in optimizing retrofitting efficiency, influencing both stress distribution mechanisms and failure progression in reinforced concrete structures.

4-1-2 Effect of concrete compressive property

The compressive strength of concrete is a crucial factor influencing the structural performance of reinforced concrete slabs, particularly in terms of load-bearing capacity, toughness, and the effectiveness of retrofitting. Higher-strength concrete, such as C45, naturally exhibits greater stiffness and resistance to localized damage, reducing the necessity for additional reinforcement. For example, the load–displacement curves of non-retrofitted C45 slabs indicate high load capacity and controlled failure progression, suggesting that retrofitting contributes only marginal improvements. Conversely, lower-strength concrete, such as C35, is more susceptible to early stiffness degradation, leading to rapid crack propagation and brittle failure. The damageT contours of non-retrofitted C35 slabs show highly concentrated damage zones, reinforcing the need for composite grid retrofitting to delay failure. Retrofitting in C35 slabs significantly enhances performance, as seen in the load–displacement diagrams of specimens like C35S1-100, which exhibit increased ultimate load and extended post-peak energy absorption. The SDEG contours further validate this effect, revealing a more uniform stiffness degradation pattern, which indicates better stress distribution and delayed failure initiation.

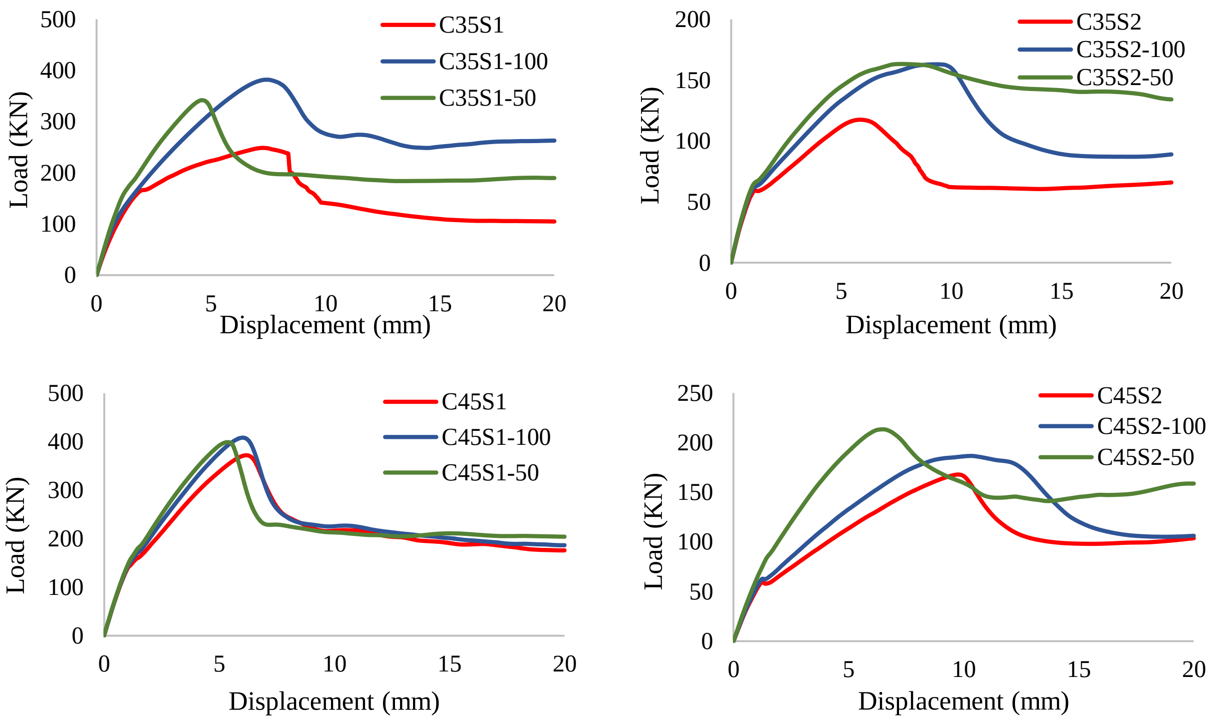

Figure 14 Load-Displacement diagram of the concrete slab specimens

These findings emphasize that while retrofitting benefits all concrete grades, the impact is far more pronounced in lower-strength slabs, highlighting the necessity of adapting retrofit strategies based on the inherent properties of the material. In other words, the efficiency of the composite grid is not just dictated by its configuration (grid opening size, reinforcement density, etc.), but also by how well its reinforcement mechanism interacts with the concrete substrate. In C45 specimens, the higher inherent strength can result in initially lower damage propagation, yet the potential for rapid, brittle failure increases. Here, the composite grid must effectively intercept and delay crack propagation to ensure ductility. The composite grid in a retrofitting system helps bridge these cracks and redistribute tensile stresses. Therefore, the degree to which the grid improves performance will inherently depend on the starting material properties of the concrete. With C45, the grid might be more focused on enhancing ductility and energy dissipation, whereas with C35 the retrofit might compensate more directly for the lower baseline tensile performance. On the other hand, in C35 specimens, the grid might have a relatively larger role in controlling crack widening and facilitating stress redistribution, since the concrete is more prone to earlier cracking. Thus, the concrete type (C35 or C45) affects both the failure mode and the retrofitting benefits offered by the composite grid.

A critical finding from the simulations is that the effectiveness of retrofitting is markedly influenced by the intrinsic properties of the concrete. For example, C35 slabs—which possess a lower compressive strength—exhibit much more pronounced damage in the non-retrofitted state, with damageT contours showing severe localization and SDEG indicators revealing rapid stiffness degradation. In one instance, the non-retrofitted C35S1 model reached ultimate load levels noticeably lower than its retrofitted counterparts, and the corresponding energy absorption was limited. Conversely, when retrofitting was applied to C35 slabs (e.g., in C35S1-50 and C35S1-100), the numerical analysis demonstrated a significant shift in behavior. The load–displacement curves for retrofitted specimens clearly showed higher ultimate loads and increased energy absorption. This enhanced performance is attributed to the reinforcement's capability to redistribute stresses more evenly, delaying the onset of catastrophic failure. In the case of the C35S1-100 model, not only did the SDEG contours display a more uniform, widespread area of stiffness degradation, but the associated load–displacement diagrams indicated that this specimen could sustain considerably higher loads, affirming that retrofitting strategies yield more dramatic improvements in lower-strength concretes.

4-1-3 Effect of grid opening size

The grid opening size plays a critical role in determining the effectiveness of retrofitting reinforced concrete slabs, particularly in how stresses are redistributed and damage is controlled. A smaller grid opening size (here 50×50) provides more localized reinforcement, effectively mitigating crack propagation in thinner slabs where stress concentrations are prominent. For example, in C35S1-50, the damageT contours indicate reduced localized damage, and the SDEG values show lower peak stiffness loss, confirming better stress confinement. Conversely, larger grid opening sizes enable wider stress redistribution across the slab, which is more effective for thicker slabs. The C35S1-100 specimen, for instance, exhibits widespread stiffness degradation in its SDEG contours, reflecting improved energy dissipation and ductility, while its load–displacement diagram shows the highest ultimate load and absorbed energy among tested configurations. These findings highlight the necessity of optimizing grid opening size based on slab thickness, ensuring localized damage control in thinner slabs while facilitating broader load distribution in thicker slabs to achieve maximum retrofitting efficiency.

The performance metrics from the bar graphs (Figures 13 and 14) indicate that the maximum load carried by C45S1-100 is noticeably higher than that of C45S1. Although the exact numerical values depend on the specific simulation output, the retrofitted sample typically exhibits an increase in load capacity by roughly 30–40% relative to the non-retrofitted slab. This improvement is more evident on the sample C35S1-100 and can be attributed to the retrofitting grid effectively redistributing tensile stresses and arresting crack propagation in the critical regions. The absorbed energy, as represented in the corresponding bar graph, shows that the retrofitted specimen absorbs a greater amount of energy before failure. This increased energy absorption (quantitatively, an improvement of around 20–30% compared to the non-retrofitted slab) reflects a higher strain energy dissipation capacity. The more uniform damage spread observed in the damageT contours of C45S1-100 supports this finding according to Table 11, as it indicates that the energy is more evenly distributed and less concentrated in vulnerable regions.

When comparing the contours at equal load levels, the C35S1-100 configuration consistently displays lower peak SDEG values, signifying that the stress is being effectively distributed. This phenomenon is reflected in the load–displacement diagrams where the C35S1-100 not only demonstrates the highest ultimate load among the C35S1 group but also absorbs the most energy among the tested configurations. The numerical investigation thereby confirms that in thicker slabs, a coarser retrofitting grid optimizes the balance between load-carrying capacity and controlled damage progression.

In these cases, the damageT and SDEG contours of C35S2-50 show that the reinforcement effectively limits the severity of localized damage. Even though the load–displacement response might not reach the same ultimate load as in thicker or coarser retrofitted cases, the improved ductility ensures that the thinner slabs are less prone to sudden brittle failure. For instance, a finer grid leads to a load–displacement curve that features a prolonged post-peak plateau, indicating gradual stiffness degradation and higher energy dissipation even if the absolute load levels are moderately lower. This clear example reinforces that thinner, lower-strength slabs benefit most from a retrofitting strategy involving a smaller grid opening, ensuring adequate control over early-age crack propagation.

It should be considered that, when each specimen reaches its individual ultimate load, the retrofitted slab's higher load capacity may lead to larger absolute areas of damage due to the higher energy input required to reach that failure state. Here, the damage contours might appear more extensive simply because the slab is experiencing greater forces, not necessarily because the retrofitting is less effective. The crucial point is that the retrofit delays the onset of critical localized damage and provides a more gradual failure progression.

The use of a perfect-bond tie constraint represents a limitation of the present numerical model. Although the experimentally validated model reproduced the principal global response with acceptable accuracy, omission of interfacial slip, progressive debonding, pull-out, and epoxy cracking may lead to an overestimation of the post-peak load and absorbed energy. Future work should incorporate experimentally calibrated cohesive-zone parameters obtained from appropriate bond or pull-off tests.

The numerical results further reveal that slab thickness, concrete compressive property, and the retrofitting grid configuration (specifically, the opening size) play pivotal roles in the overall structural behavior.

4-2 Limitation of the study

The numerical model assumed a perfect bond between the braided composite grid and the concrete surface. Consequently, interfacial slip, progressive debonding, epoxy cracking, and grid pull-off were not explicitly represented. This assumption is one reason why the numerical model overestimated the post-peak residual load and absorbed energy of specimen C35S1-50. In addition, experimental validation was limited to the C35S1 control specimen and the C35S1-50 retrofitted specimen. The responses of the C45 slabs, the 65 mm-thick slabs, and the specimens retrofitted with a 100×100 mm grid remain numerical predictions. Only two slab thicknesses and two grid-opening sizes were investigated; therefore, the results demonstrate trends within the selected parameter range rather than defining a universally optimal configuration. The tests were also performed under monotonic short-term loading, and the effects of cyclic loading, fatigue, environmental exposure, and long-term bond degradation require further investigation.

5 Conclusion

This research comprehensively investigates the impact of braided composite grid on the load-bearing capacity and fracture behavior of RC concrete slabs. By utilizing a previously developed RVE model, the study analyzed its behavior under concentric loading subjected to the retrofitted concrete slab. The results from experimental and numerical tests demonstrated strong consistency, confirming the reliability of the numerical model.

For the retrofitted specimen, the differences between the experimental and numerical results were 5.57% for ultimate load, 1.33% for deflection at ultimate load, and 5.87% for absorbed energy. The experimental damage patterns also showed qualitative agreement with the numerical tensile-damage and stiffness-degradation distributions, supporting the suitability of the adopted multiscale modeling approach for comparative structural assessment. The braided composite grids improved load-carrying capacity, absorbed energy, and damage distribution. Within the investigated configurations, the ultimate load and absorbed energy increased by up to 53.62% and 70.70%, respectively, relative to the corresponding unretrofitted control slabs. The results provide a strong foundation for further research and practical applications in the field of structural engineering. The grid study validated the finite element model's performance, ensuring accurate simulation results. These findings underscore the braided composite grid's efficacy in retrofitting concrete slabs, offering a promising solution for improving structural performance and durability.

This numerical investigation has demonstrated that the structural performance of reinforced concrete slabs retrofitted with a braided composite grid is significantly influenced by slab thickness, concrete compressive strength, and grid opening size. The results reveal that thicker slabs exhibit inherently superior load-bearing capacity and toughness, rendering the retrofitting effect more pronounced in thinner configurations, especially in lower-strength concrete such as C35. While higher-strength concrete (C45) benefits less from retrofitting due to its intrinsic resistance to localized damage, C35 slabs experience substantial improvements, with enhanced ultimate load and energy absorption. The results also showed that the influence of grid opening depended on slab thickness and concrete strength. The 100×100 mm configuration generally produced greater improvements for the 105 mm-thick slabs, whereas the denser 50×50 mm grid was more effective for the 65 mm-thick slabs, particularly in terms of absorbed energy. Therefore, grid density should be selected in relation to the mechanical properties and geometry of the concrete substrate rather than considered independently. The findings confirm that retrofitting effectiveness is highly dependent on the interaction between material properties and geometric configurations, highlighting the necessity for tailored design approaches that optimize reinforcement strategies based on specific structural requirements. Interpreting the results using SDEG and damageT contour plots provides valuable insights into the failure mechanisms and damage progression within the RC slab model. Future research could explore experimental verification of the numerical model and also the long-term performance and durability of retrofitted slabs under various environmental conditions and loading scenarios. Additionally, investigating other composite materials and grid configurations could provide further insights into optimizing retrofitting strategies.

REFERENCES

[1] G. Santana and A. C. I. Committee, Building Code Requirements for Structural Concrete (ACI 318-19) and Commentary. 2019.

[2] S. Fareed, Behavior of reinforced concrete slabs under accidental impacts. 2018.

[3] S. M. Anas, M. Alam, and M. Saidani, "Prediction of impact response of square reinforced concrete (RC) slab with square/circular opening under drop-weight impact using FEM simulation," Asian Journal of Civil Engineering, vol. 25, no. 2, pp. 2189-2208, 2024/02/01 2024, doi: 10.1007/s42107-023-00903-y.

[4] "Developments in Civil Engineering," in Fiber-Reinforced-Plastic (FRP) Reinforcement for Concrete Structures, A. Nanni Ed. Oxford: Elsevier, 1993, p. ii.

[5] T. Triantafillou, "Innovative Textile-Based Cementitious Composites for Retrofitting of Concrete Structures," 2011, pp. 209-223.

[6] Q. Ngo and H.-C. Nguyen, "Experimental and Numerical Investigations on Flexural Behaviour of Prestressed Textile Reinforced Concrete Slabs," Civil Engineering Journal, vol. 7, pp. 1084-1097, 06/02 2021, doi: 10.28991/cej-2021-03091712.

[7] P. Monteiro and P. Mehta, Concrete: Microstructure, Properties and Materials. 2006.

[8] G. F. Limbrunner and A. O. Aghayere, Reinforced Concrete Design. Pearson/Prentice Hall, 2010.

[9] H. Ni and R. S. Aboutaha, "Numerical Study of Prestressed Concrete Girder-Deck System with Variable Reinforcement and Span-depth Ratios," in Proceedings of The 17th East Asian-Pacific Conference on Structural Engineering and Construction, 2022, Singapore, G. Geng, X. Qian, L. H. Poh, and S. D. Pang, Eds., 2023// 2023: Springer Nature Singapore, pp. 1387-1400.

[10] P. Balaguru, A. Nanni, and J. Giancaspro, FRP Composites for Reinforced and Prestressed Concrete Structures: A Guide to Fundamentals and Design for Repair and Retrofit. 2008.

[11] A. Monserrat-López, I. Josa, S. Aidarov, P. Pujadas, and A. de la Fuente, "Sustainability of column-supported slabs for buildings: A multi-criteria assessment," Structural Concrete, vol. n/a, no. n/a, doi: https://doi.org/10.1002/suco.202400769.

[12] A. Altemen, M. t. Medhlom, and M. Özakça, "Structural Behavior of Full-Scale Novel Hybrid Layered Concrete Slabs Reinforced with CFRP and Steel Grids under Impact Load," Buildings, vol. 14, p. 2625, 08/24 2024, doi: 10.3390/buildings14092625.

[13] R. Suwondo, L. Cunningham, M. Keintjem, and M. Suangga, "Evaluating environmental sustainability in concrete slabs: a comparative study of embodied carbon for different design approaches," Asian Journal of Civil Engineering, vol. 25, pp. 1-10, 02/29 2024, doi: 10.1007/s42107-024-01002-2.

[14] R. Suwondo, L. Cunningham, M. Keintjem, and M. Suangga, "Evaluating environmental sustainability in concrete slabs: a comparative study of embodied carbon for different design approaches," Asian Journal of Civil Engineering, vol. 25, no. 4, pp. 3655-3664, 2024/06/01 2024, doi: 10.1007/s42107-024-01002-2.

[15] L. Pelà, A. Aprile, and A. Benedetti, "Experimental study of retrofit solutions for damaged concrete bridge slabs," Composites Part B: Engineering, vol. 43, no. 5, pp. 2471-2479, 2012/07/01/ 2012, doi: https://doi.org/10.1016/j.compositesb.2011.08.038.

[16] M. Abedi, O. Hassanshahi, J. A. O. Barros, A. Gomes Correia, and R. Fangueiro, "Three-dimensional braided composites as innovative smart structural reinforcements," Composite Structures, vol. 297, p. 115912, 2022/10/01/ 2022, doi: https://doi.org/10.1016/j.compstruct.2022.115912.

[17] A. S. Soureh, M. S. Johari, and S. K. Ilkhechi, "Investigating the effect of fiber arrangement on tensile properties of two-dimensional hybrid braided composite rods," Scientific Reports, vol. 15, no. 1, p. 3116, 2025.

[18] C. Ayranci and J. Carey, "Predicting the longitudinal elastic modulus of braided tubular composites using a curved unit-cell geometry," Composites Part B: Engineering, vol. 41, pp. 229-235, 04/01 2010, doi: 10.1016/j.compositesb.2009.10.006.

[19] S. M. Raoof, L. N. Koutas, and D. A. Bournas, "Bond between textile-reinforced mortar (TRM) and concrete substrates: Experimental investigation," Composites Part B: Engineering, vol. 98, pp. 350-361, 2016.

[20] E. del Rey Castillo, A. Niroomandi, and T. Triantafillou, "Seismic Retrofitting of Realistic Beam–Column Joints with Shear Failure Using FRP Sheets and FRP Anchors," Journal of Composites for Construction, vol. 28, no. 4, p. 05024001, 2024.

[21] S. Omairey, P. Dunning, and S. Sriramula, "Development of an ABAQUS plugin tool for periodic RVE homogenisation," Engineering With Computers, vol. 35, 04/01 2019, doi: 10.1007/s00366-018-0616-4.

[22] S. Al Hasani, H. Nasrellah, and A. A. Abdulraeg, "Numerical study of reinforced Concrete beam by using ABAQUS software," International Journal of Innovative Technology and Interdisciplinary Sciences, vol. 4, no. 3, pp. 733-741, 2021.

[23] Z. Liu, C. Wu, B. Ren, W. K. Liu, and R. Grimes, "Multiscale simulations of material with heterogeneous structures based on representative volume element techniques," in 15th international LS-DYNA users conference, 2018, pp. 1-10.

[24] A. Gholami and G. W. Melenka, "Finite element analysis of 2-D tubular braided composite based on geometrical models to study mechanical performances," Mechanics of Advanced Materials and Structures, vol. 29, no. 28, pp. 7542-7558, 2022/12/16 2022, doi: 10.1080/15376494.2021.2001879.

[25] P. Qu, X. Guan, Y. Jia, S. Lou, and J. Nie, "Effective elastic properties and stress distribution of 2D biaxial nonorthogonally braided composites," Journal of Composite Materials - J COMPOS MATER, vol. 46, pp. 997-1008, 04/01 2012, doi: 10.1177/0021998311413684.

[26] A. K. Pickett, J. Sirtautas, and A. Erber, "Braiding Simulation and Prediction of Mechanical Properties," Applied Composite Materials, vol. 16, no. 6, pp. 345-364, 2009/12/01 2009, doi: 10.1007/s10443-009-9102-x.

[27] A. Shakersoureh, M. Safarjohari, H. Dabiryan, F. Hatami, and F. Biglari, "Prediction of elastic properties for 2D biaxial and triaxial braided composites using a multiscale

RVE-FEM framework," Results in Engineering, vol. 30, p. 110558, 2026/06/01/ 2026, doi: https://doi.org/10.1016/j.rineng.2026.110558.

[28] L. N. Koutas and D. A. Bournas, "Flexural Strengthening of Two-Way RC Slabs with Textile-Reinforced Mortar: Experimental Investigation and Design Equations," Journal of Composites for Construction, vol. 21, no. 1, p. 04016065, 2017, doi: doi:10.1061/(ASCE)CC.1943-5614.0000713.

[29] Z. Deng, Q. Xia, M. Gong, and J. Xu, "Flexural Strengthening of Two-Way RC Slabs with Textile Reinforced Mortar: Experimental Study and Calculation Model," KSCE Journal of Civil Engineering, vol. 27, no. 12, pp. 5268-5280, 2023/12/01/ 2023, doi: https://doi.org/10.1007/s12205-023-2174-6.

[30] H.-Y. Kim, Y.-J. You, G.-S. Ryu, K.-T. Koh, G.-H. Ahn, and S.-H. Kang, "Flexural Strengthening of Concrete Slab-Type Elements with Textile Reinforced Concrete," Materials, vol. 13, no. 10, p. 2246, 2020. [Online]. Available: https://www.mdpi.com/1996-1944/13/10/2246.

[31] L. Fang, Y. Zhou, D. Yi, and W. Yi, "Experimental Study on Flexural Capacity of Corroded RC Slabs Reinforced with Basalt Fiber Textile," Applied Sciences, vol. 11, no. 1, p. 144, 2021. [Online]. Available: https://www.mdpi.com/2076-3417/11/1/144.

[32] P. Potluri, A. Rawal, M. Rivaldi, and I. Porat, "Geometrical modelling and control of a triaxial braiding machine for producing 3D preforms," Composites Part A: Applied Science and Manufacturing, vol. 34, no. 6, pp. 481-492, 2003/06/01/ 2003, doi: https://doi.org/10.1016/S1359-835X(03)00061-7.

[33] A. Nanni, M. J. Henneke, and T. Okamoto, "Tensile properties of hybrid rods for concrete reinforcement," Construction and Building Materials, vol. 8, no. 1, pp. 27-34, 1994/01/01/ 1994, doi: https://doi.org/10.1016/0950-0618(94)90005-1.

[34] H. Saraswat, A. Rawal, and R. Singh, "Tensile behaviour of multi-layered braided structures," Journal of Materials Science, vol. 49, no. 18, pp. 6427-6436, 2014/09/01 2014, doi: 10.1007/s10853-014-8372-3.

[35] Y. Kyosev, "Braiding Technology for Textiles," ed: Woodhead Publishing, 2014.

[36] M. Hafezolghorani, F. Hejazi, R. Vaghei, M. S. B. Jaafar, and K. Karimzade, "Simplified damage plasticity model for concrete," Structural engineering international, vol. 27, no. 1, pp. 68-78, 2017.

[37] A. Rehman, A. Masood, S. Akhtar, S. M. Ibrahim, and M. Shariq, "Experimental and numerical investigation into flexural bond strength of RC beams exposed to elevated temperature," Construction and Building Materials, vol. 282, p. 122630, 2021/05/03/ 2021, doi: https://doi.org/10.1016/j.conbuildmat.2021.122630.

[38] G. M. Chen, J. F. Chen, and J. G. Teng, "On the finite element modelling of RC beams shear-strengthened with FRP," Construction and Building Materials, vol. 32, pp. 13-26, 2012/07/01/ 2012, doi: https://doi.org/10.1016/j.conbuildmat.2010.11.101.

[39] C. Coronado and M. López, "Sensitivity analysis of reinforced concrete beams strengthened with FRP laminates," Cement & Concrete Composites - CEMENT CONCRETE COMPOSITES, vol. 28, pp. 102-114, 01/31 2006, doi: 10.1016/j.cemconcomp.2005.07.005.

[40] O. Ali, A. Abbas, E. Khalil, and H. Madkour, "Numerical investigation of FRP-confined short square RC columns," Construction and Building Materials, vol. 275, p. 122141, 2021/03/15/ 2021, doi: https://doi.org/10.1016/j.conbuildmat.2020.122141.

[41] A. Raza, A. u. Rehman, B. Masood, and I. Hussain, "Finite element modelling and theoretical predictions of FRP-reinforced concrete columns confined with various FRP-tubes," Structures, vol. 26, pp. 626-638, 2020/08/01/ 2020, doi: https://doi.org/10.1016/j.istruc.2020.04.033.

[42] J.-Q. Yang, S. T. Smith, Z. Wang, and Y. Y. Lim, "Numerical simulation of FRP-strengthened RC slabs anchored with FRP anchors," Construction and Building Materials, vol. 172, pp. 735-750, 2018/05/30/ 2018, doi: https://doi.org/10.1016/j.conbuildmat.2018.03.133.

[43] A. S. Genikomsou and M. A. Polak, "Finite element analysis of punching shear of concrete slabs using damaged plasticity model in ABAQUS," Engineering Structures, vol. 98, pp. 38-48, 2015/09/01/ 2015, doi: https://doi.org/10.1016/j.engstruct.2015.04.016.